THE JOURNAL OF PHYSICAL CHEMISTRY C
A JOURNAL OF THE AMERICAN CHEMICAL SOCIETY

pubs.acs.org/JPCC

Article

Lattice Kerker Effect with Plasmonic Oligomers

Published as part of The Journal of Physical Chemistry virtual special issue "125 Years of The Journal of Physical Chemistry".

Marc R. Bourgeois, Andrew W. Rossi, Matthieu Chalifour, Charles Cherqui, and David J. Masiello*

Cite This: https://doi.org/10.1021/acs.jpcc.1c05024

Read Online

ACCESS | Metrics & More | Article Recommendations | Supporting Information

ABSTRACT: The lattice Kerker effect refers to a strong suppression of reflected light from periodic arrays of scatterers in narrow spectral windows at normal incidence. It can occur when interference of scattered light from different multipolar modes from each unit cell and diffractive coupling among unit cells occur simultaneously. Here we investigate manifestations of the lattice Kerker effect in 1D arrays of planar plasmonic oligomer trimers. Numerical results computed using a coupled electric dipole model for 1D non-Bravais trimer arrays, where the three constituent particles in each trimer unit cell are explicitly included, are rationalized using a coupled electric and magnetic dipole model on a 1D Bravais lattice. This model allows the differential scattered power angular distributions from the array to be decomposed into the product of the angular distribution produced by a single unit cell containing colocalized electric and magnetic dipoles and the squared modulus of a structure factor accounting for diffraction arising from the periodic array. In addition to providing an intuitive explanation for characteristic signatures of the lattice Kerker effect at normal incidence, this model also enables the facile evaluation of angular scattered power distributions for non-normal angles of incidence. The results of this work expand the concept of the lattice Kerker effect in terms of both unit cell design and excitation conditions and provide a simple analytic model for designing periodic structures with engineered properties for applications in nanophotonics concerned with highly directional radiation beaming and enhanced magnetic field strengths at optical frequencies.

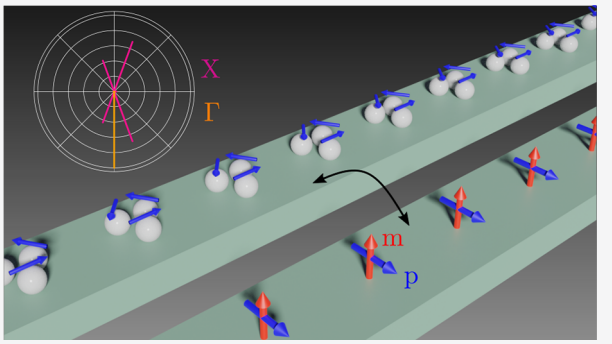

INTRODUCTION

In 1983, Kerker and co-workers used Mie theory to study electromagnetic scattering from spherical particles with nonunity relative permittivity ε and permeability μ.[1] They pointed out that, under the condition $\varepsilon = \mu$, perfect destructive interference of light scattered by the electric and magnetic multipoles of each order occurs in the backward direction, leading to a strong asymmetry in the electromagnetic power scattered into the forward versus backward directions. The simplest situation satisfying such a condition, termed the first Kerker condition, consists of spectrally overlapped electric (ED) and magnetic dipole (MD) resonances.[2] While interesting from a theoretical perspective, the lack of natural materials possessing $\mu(\omega) \neq 1$ at frequencies higher than ∼1 GHz initially precluded leveraging this result to exert control over the direction of optical radiation.[3] However, in the past two decades there has been an enormous resurgence of interest in the Kerker effect owing to the discovery of nanoscale dielectric particles[4,5] and plasmonic oligomer structures[6−11]—cyclic assemblies of plasmonic nanoparticles (NPs)—capable of achieving strong MD scattering at visible and near-IR frequencies.

Generalizations of the Kerker effect have also emerged; the asymmetric forward versus backward scattering arising from same-order multipoles originally discussed by Kerker has also been demonstrated using interferences between multipoles of different order.[2,12,13] The identity of the excitation source also influences the angular distribution of scattered radiation as observed in directional beaming from single plasmonic NPs supporting quadrupolar and higher-order multipoles excited by a focused electron beam and detected via cathodoluminescence.[14] Beyond the scattering properties of individual dielectric or plasmonic oligomer systems, there has been much interest in studying periodic arrays of NPs. In particular, a generalized Brewster effect in dielectric metasurfaces has been identified, which allows for linearly polarized reflection from an array of silicon nanodisks at visible wavelengths.[15]

Received: June 7, 2021
Revised: August 6, 2021

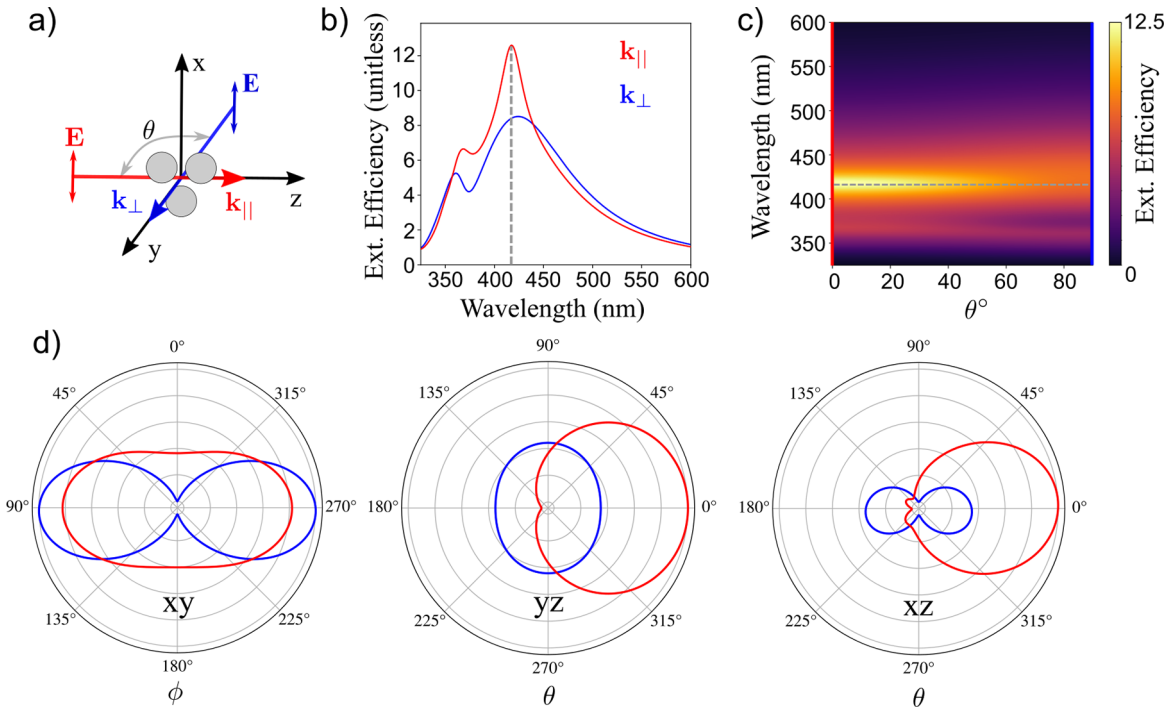

Figure 1. Isolated trimer far-field observables. (a) Illustration of the trimer structure (80 nm diameter Ag spheres with 10 nm surface-to-surface gaps) situated in the *xz*-plane. Two excitation geometries with *x*-polarized electric fields and wave vectors parallel $\mathbf{k}_{\parallel}$ and perpendicular $\mathbf{k}_{\perp}$ to the trimer plane are shown in red and blue, respectively. (b) Extinction efficiency spectra for $\mathbf{k}_{\parallel}$ and $\mathbf{k}_{\perp}$ excitation geometries indicated in panel (a). (c) Extinction efficiency surface plot as the excitation angle θ is varied continuously between $\mathbf{k}_{\parallel}$ and $\mathbf{k}_{\perp}$ showing the smooth introduction of the MD mode near λ = 415 nm (dashed). (d) Angular scattering plots illustrating the spatial distribution of light scattered within the three Cartesian planes following excitation by $\mathbf{k}_{\parallel}$ and $\mathbf{k}_{\perp}$ cases. Each plot is normalized to the maximum scattered power from either $\mathbf{k}_{\parallel}$ and $\mathbf{k}_{\perp}$ cases. The forward beaming of radiation along the $\hat{\mathbf{z}}$-direction is the characteristic signature of MD excitation and the Kerker effect.

Split-ring resonator arrays[16] and dielectric metasurfaces[17,18] exhibiting ED and MD coupling have also enabled exquisite control of light propagation. In the diffractively coupled regime, lattice modes arise from the hybridization of ED and MD moments excited at each lattice site with the photonic modes dictated by the underlying lattice periodicity. The so-called lattice Kerker effect (LKE)[19] has been demonstrated in this regime, signified by near-vanishing reflection in spectral windows where the diffractively coupled ED and MD lattice modes spectrally overlap. While this idea was originally studied in the context of 2D arrays of dielectric NPs supporting ED and MD modes,[19] generalizations of the LKE have recently appeared in the literature with unit cells containing individual plasmonic NPs with quadrupolar electric and magnetic multipoles strongly contributing to the scattering properties.[20,21] There have been comparatively few studies of periodic arrays with plasmonic oligomer unit cells featuring strong near-field coupling[22−25] and none, to the best of our knowledge, explicitly concerning the LKE despite the possibility of realizing strong ED and MD modes in such systems. Furthermore, previous studies of the LKE have considered only the normally incident excitation case,[19−21] while there has been a recent push in the literature toward understanding the behavior of lattice systems at nonzero angles of incidence in terms of the underlying band structure inherited from the array periodicity.[26−30]

Here we show that 1D periodic arrays of plasmonic trimer oligomers exhibit the characteristic signatures of the LKE at the Γ point and extend the LKE concept to other high symmetry points in reciprocal space. In contrast to previous LKE studies that considered Bravais lattices with a single site per unit cell with isotropic MD polarizability tensors, non-Bravais plasmonic lattices are considered in this work. The planar nature of the plasmonic oligomer structures introduces strict symmetry restrictions on the excitation of MD lattice modes via the highly anisotropic MD polarizability tensor associated with each unit cell. The resulting MD excitation angular dependence motivates the investigation of the LKE at nonzero angles of incidence. We show that the decoupling of diffractively coupled ED and MD lattice modes underlying previous observations of the LKE are also realized at each of the high-symmetry points in reciprocal space. Directional beaming effects from 1D arrays of plasmonic trimer oligomers are investigated numerically using the coupled ED and the coupled ED-MD models on non-Bravais and Bravais lattices, respectively. Scattered radiation beaming arising in the context of the LKE are analytically related to the more well-known Kerker effect.

RESULTS AND DISCUSSION

Individual Trimer Response. Before investigating manifestations of the LKE in the context of periodic arrays with plasmonic oligomer unit cells, the optical response of an isolated oligomer is first considered. In contrast to the case of high-index dielectric scatterers where ED and MD modes are often nondegenerate,[5,31] the spectral detuning between the ED and MD modes supported by oligomers composed of plasmonic building blocks are more controllable.[10,11,32,33] Throughout this work a single planar plasmonic trimer structure is considered, consisting of 80 nm diameter Ag nanoparticles with 10 nm surface-to-surface gaps embedded in an environment with unity refractive index. The optical

https://doi.org/10.1021/acs.jpcc.1c05024
J. Phys. Chem. C XXXX, XXX, XXX−XXX

response of the system is evaluated in the dipole limit, where each sphere is represented as a point ED with moment $\mathbf{p}_j$. The ED moment vectors within the optically excited trimer are determined by solving the coupled dipole system of equations

$$\overleftrightarrow{\alpha}_p^{-1}\cdot\mathbf{p}_j = \mathbf{E}_0(\mathbf{r}_j) + \mu k_0^2 \sum_{l\neq j} \overleftrightarrow{G}(\mathbf{r}_j, \mathbf{r}_l)\cdot\mathbf{p}_l \tag{1}$$

where $\mathbf{E}_0(\mathbf{r}_j)$ is the incident plane wave field and the second term on the right-hand-side of eq 1 is the scattered field from the other $l \neq j$ EDs in the system. Electromagnetic coupling between EDs is determined by the full dipole−dipole relay tensor

$$\overleftrightarrow{G}(\mathbf{r}_j, \mathbf{r}_l) = \frac{e^{ikR_{jl}}}{R_{jl}}\left[\left(1 + \frac{i}{kR_{jl}} - \frac{1}{(kR_{jl})^2}\right)\overleftrightarrow{I} + \left(-1 - \frac{3i}{kR_{jl}} + \frac{3}{(kR_{jl})^2}\right)\hat{\mathbf{R}}_{jl}\hat{\mathbf{R}}_{jl}\right] \tag{2}$$

where $k_0 = 2\pi/\lambda$ is the wave vector magnitude in vacuum, $k = k_0 n$ is the magnitude of the wave vector inside the embedding medium with refractive index $n = \sqrt{\varepsilon\mu}$, and $\mathbf{R}_{jl} = \mathbf{r}_j - \mathbf{r}_l$. Fully retarded ED polarizability tensors $\overleftrightarrow{\alpha}_p(\omega)$ for the spherical particles considered were evaluated using the a_1 scattering coefficient from Mie theory with the Ag dielectric function data of Johnson and Christy.[34]

Figure 1a shows the trimer structure oriented in the *xz*-plane as well as two different plane wave excitation geometries, both polarized along $\hat{\mathbf{x}}$ but with incident wave vectors parallel $\mathbf{k}_\parallel$ (red) and perpendicular $\mathbf{k}_\perp$ (blue) to the trimer plane. Previous works[7,8] have demonstrated that while only the ED modes are accessible under the $\mathbf{k}_\perp$ excitation case, both ED and MD modes are accessible for the $\mathbf{k}_\parallel$ case. Extinction efficiency spectra for the two excitation geometries considered are presented in Figure 1b. The lowest-energy feature in the extinction spectrum associated with the perpendicular excitation case is expected to be purely electric dipolar in nature. Under the parallel excitation geometry, an additional nearly degenerate mode is evident arising from the MD. Although the MD modes of related structures have often appeared at lower energies compared to the ED modes,[7,8] the near-degeneracy observed in the present case is attributed to the comparatively larger surface-to-surface gaps used in this work.

The scattered power radiated into direction $\hat{\mathbf{n}}'$ by a pair of ED $\mathbf{p}$ and MD $\mathbf{m}$ sources colocated at the origin can be expressed, in Gaussian units, as

$$\frac{dP_0(\hat{\mathbf{n}}')}{d\Omega} = \frac{ck_0^4\mu n^2}{8\pi}\mathrm{Re}\left\{\frac{1}{n}[|\mathbf{p}|^2 - (\hat{\mathbf{n}}'\cdot\mathbf{p})(\hat{\mathbf{n}}'\cdot\mathbf{p}^*)] + n[|\mathbf{m}|^2 - (\hat{\mathbf{n}}'\cdot\mathbf{m})(\hat{\mathbf{n}}'\cdot\mathbf{m}^*)] + \hat{\mathbf{n}}'\cdot[(\mathbf{p}\times\mathbf{m}^*) + (\mathbf{p}^*\times\mathbf{m})]\right\} \tag{3}$$

When only $\mathbf{p}$ or $\mathbf{m}$ is nonzero, the resulting differential scattered power profiles exhibit the characteristic $\sin^2\theta$ dependence, with θ measured from the direction of the dipole moment. Indeed, under $\mathbf{k}_\perp$ excitation, the angular distributions calculated using the coupled dipole method for the trimer structure in Figure 1d closely match that produced by a single ED along the $\hat{\mathbf{x}}$ direction. In contrast, the angular distributions under $\mathbf{k}_\parallel$ excitation (red) show the strong forward beaming along the $\hat{\mathbf{z}}$ direction indicative of the Kerker effect and simultaneous ED and MD excitation.

In a planar trimer oligomer, there are two orthogonal dipole moments in the trimer plane per constituent NP, leading to the existence of six normal modes in what is referred to herein as the trimer basis. These trimer normal modes are enumerated in Figure 2a and labeled as longitudinal (transverse) if the constituent dipole moments are parallel (perpendicular) to the legs of the equilateral triangle with trimer NPs at the midpoint of each leg. The longitudinal normal modes consist of a single MD mode, with a head-to-tail arrangement of constituent EDs, along with two degenerate ED modes. Of the three transverse modes, two are degenerate ED modes and the third is an optically dark "breathing" mode with net zero electric dipole moment. Of the two pairs of doubly degenerate ED trimer modes, those comprising transverse (longitudinal) dipoles are of lower (higher) energy.[7] While this is the energetic ordering of modes for spherical NPs, previous works investigating MD modes supported by nanorod trimers have employed high aspect-ratio rods to influence the spectral detuning and energetic ordering of these two classes of trimer modes in order to decongest the resulting spectra in the vicinity of the MD mode.[10,35,36]

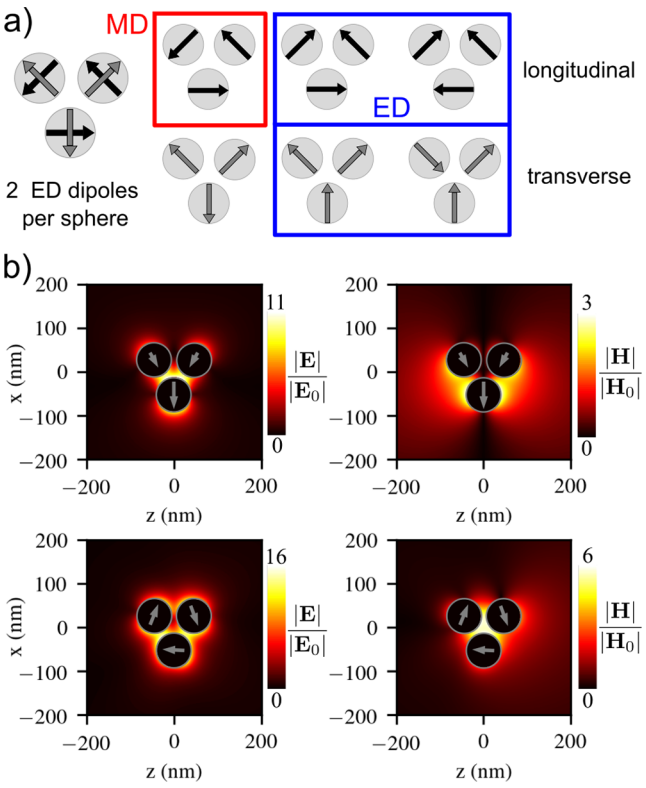

Figure 2. Individual trimer response. (a) Schematic representation of ED orientations in the six trimer normal modes composed of in-plane EDs supported by each constituent Ag sphere. (b) Electric (left) and magnetic (right) field distributions in the near-field region of the isolated trimer system excited under the $\mathbf{k}_\perp$ (top) and $\mathbf{k}_\parallel$ (bottom) conditions depicted in Figure 1a with λ = 415 nm. Gray arrows within the NP interiors indicate the relative magnitudes and orientations of the induced dipole moments.

https://doi.org/10.1021/acs.jpcc.1c05024
J. Phys. Chem. C XXXX, XXX, XXX−XXX

Once the induced ED moments within the trimer have been determined using the coupled ED method, the spatial distribution of the electric response field is evaluated as

$$\mathbf{E}(\mathbf{r}) = \mu k_0^2 \sum_l \vec{\mathbf{G}}(\mathbf{r}, \mathbf{r}_l)\cdot\mathbf{p}_l \tag{4}$$

where l ranges over all dipoles in the system. The spatial distribution of the magnetic response field is similarly evaluated as

$$\mathbf{H}(\mathbf{r}) = -ik_0 \sum_l \mathbf{g}(\mathbf{r}, \mathbf{r}_l) \times \mathbf{p}_l \tag{5}$$

where

$$\mathbf{g}(\mathbf{r}, \mathbf{r}_l) = \frac{e^{ik|\mathbf{r}-\mathbf{r}_l|}}{|\mathbf{r}-\mathbf{r}_l|}\left(\frac{ik}{|\mathbf{r}-\mathbf{r}_l|} - \frac{1}{|\mathbf{r}-\mathbf{r}_l|^2}\right)(\mathbf{r}-\mathbf{r}_l) \tag{6}$$

Spatial distributions of the electric and magnetic fields were calculated within the xz-plane in the near-field region of the trimer system for the $\mathbf{k}_\parallel$ and $\mathbf{k}_\perp$ excitation conditions shown in Figure 1a and an incident wavelength of λ = 415 nm (Figure 2b). The gray arrows superimposed on the electric and magnetic field maps indicate the orientations and magnitudes of the induced EDs on each sphere. The top panel of Figure 2b shows that, in the perpendicular excitation geometry (blue in Figure 1), one of the two degenerate transverse trimer ED dipole modes is primarily excited, setting up a net electric dipole along the $\hat{\mathbf{x}}$ direction with modest enhancement of the magnetic field. The lower panel of Figure 2b shows that when the trimer is excited in the parallel excitation geometry (red in Figure 1), the electric field is enhanced in the gap regions between NPs with a head-to-tail arrangement of induced electric dipoles characteristic of a y-oriented MD mode. This assignment is further validated by the observed enhancement of the magnetic field at the center of the trimer. Spectral and spatial field calculations performed using the coupled ED method were validated against results from version 3 of the MSTM T-Matrix code[37,38] with a dipole-restricted vector spherical harmonic basis. Additional T-Matrix calculations performed using an expanded multipolar basis set exhibited a slight red-shift in the spectral positions of the trimer oligomer modes, though the spectral and field plot features remained in clear qualitative agreement with all results presented in the main text (Supporting Information).

1D Periodic Arrays: Theoretical Modeling. Having investigated the electromagnetically coupled modes supported by the isolated trimer structure, the present section considers 1D periodic arrays where each unit cell contains a single plasmonic trimer. While on the one hand such a structure may be viewed as a 1D non-Bravais lattice with three sites per unit cell, the same structure may be alternatively viewed as a 1D Bravais lattice where the single site at the center of each unit cell hosts both electric and magnetic dipole modes. The later viewpoint establishes the connection between the present work and previous studies of various realizations of the LKE.[19−21]

Taking this perspective, the coupled ED and MD equations can be expressed in site space as[20]

$$\begin{aligned}\vec{\boldsymbol{\alpha}}_p^{-1}\cdot\mathbf{p}_j &= \mathbf{E}_0(\mathbf{r}_j) + \mu k_0^2 \sum_{l\neq j} \vec{\mathbf{G}}_{jl}\cdot\mathbf{p}_l + i\mu k_0 \sum_{l\neq j} (\mathbf{g}_{jl}\times\mathbf{m}_l)\\ \vec{\boldsymbol{\alpha}}_m^{-1}\cdot\mathbf{m}_j &= \mathbf{H}_0(\mathbf{r}_j) + n^2 k_0^2 \sum_{l\neq j} \vec{\mathbf{G}}_{jl}\cdot\mathbf{m}_l - ik_0 \sum_{l\neq j} (\mathbf{g}_{jl}\times\mathbf{p}_l)\end{aligned} \tag{7}$$

where $\mathbf{p}_j$ and $\mathbf{m}_j$ represent the colocalized trimer basis electric and magnetic dipole moments at the center of the jth unit cell with effective polarizability tensors $\vec{\boldsymbol{\alpha}}_p(\omega)$ and $\vec{\boldsymbol{\alpha}}_m(\omega)$, respectively. Note that the $i = j$ terms are excluded from each sum in eq 7 since the ED and MD modes are eigenmodes supported by each trimer and, therefore, do not couple within the same unit cell. ED−ED and MD−MD coupling between timers in the jth and lth unit cells is dictated by the full dipole−dipole relay tensor $\vec{\mathbf{G}}_{jl} = \vec{\mathbf{G}}(\mathbf{r}_j, \mathbf{r}_l)$ given in eq 2, while ED−MD cross coupling is determined by the vector $\mathbf{g}_{jl} = \mathbf{g}(\mathbf{r}_j, \mathbf{r}_l)$ defined in eq 6. The 1D periodicity is taken along the $\hat{\mathbf{x}}$-direction such that $\mathbf{R}_{jl} = R_{jl}\hat{\mathbf{R}}_{jl} = (j-l)a\hat{\mathbf{x}}$.

Moving into reciprocal space using the Bloch wave ansatz $\boldsymbol{\xi}_l = \boldsymbol{\xi}_{k_\parallel} e^{ik_\parallel r_l}$ with $\boldsymbol{\xi} = \mathbf{p}$, $\mathbf{m}$ and Bloch vector magnitude $k_\parallel$ contained within the first Brillouin zone, the coupled set of equations in eq 7 become

$$\begin{aligned}\vec{\boldsymbol{\alpha}}_p^{-1}\cdot\mathbf{p}_{k_\parallel} &= \mathbf{E}_{0k_\parallel} + \mu k_0^2 \vec{\mathbf{S}}(k_\parallel)\cdot\mathbf{p}_{k_\parallel} + i\mu k_0 \vec{\mathbf{T}}(k_\parallel)\cdot\mathbf{m}_{k_\parallel}\\ \vec{\boldsymbol{\alpha}}_m^{-1}\cdot\mathbf{m}_{k_\parallel} &= \mathbf{H}_{0k_\parallel} + n^2 k_0^2 \vec{\mathbf{S}}(k_\parallel)\cdot\mathbf{m}_{k_\parallel} - ik_0 \vec{\mathbf{T}}(k_\parallel)\cdot\mathbf{p}_{k_\parallel}\end{aligned} \tag{8}$$

The lattice sum tensor $\vec{\mathbf{S}}(k_\parallel) = \sum_{l\neq 0} \vec{\mathbf{G}}_{0l} e^{ik_\parallel a l}$ determines ED−ED and MD−MD coupling, while

$$\vec{\mathbf{T}}(k_\parallel) = \sum_{l\neq 0} \begin{pmatrix} 0 & -g_{0l}^z & g_{0l}^y \\ g_{0l}^z & 0 & -g_{0l}^x \\ -g_{0l}^y & g_{0l}^x & 0 \end{pmatrix} e^{ik_\parallel a l} \tag{9}$$

is the ED−MD coupling tensor. Note that the global origin has been defined as the center of the $j = 0$ unit cell. It is clear from eq 6 that only the x-component of g_{0l} is nonzero since $\mathbf{R}_{0l} \propto \hat{\mathbf{x}}$. Thus, $\vec{\mathbf{T}}(k_\parallel)$ couples only the z- and y-components of the electric and magnetic dipoles. In this case, eqs 6 and 9 can be used to write the only remaining independent element of ED−MD coupling tensor as

$$\begin{aligned}T_{zy}(k_\parallel) &= -\sum_{l\neq 0} \frac{e^{ika|l|}}{|l|}\left(\frac{ik}{a|l|} - \frac{1}{a^2|l|^2}\right) l e^{ik_\parallel a l}\\ &= -\sum_{l>0} e^{ikal}\left(\frac{ik}{al} - \frac{1}{a^2 l^2}\right)\left(e^{ik_\parallel a l} - e^{-ik_\parallel a l}\right)\\ &= -2i\sum_{l>0} e^{ikal}\left(\frac{ik}{al} - \frac{1}{a^2 l^2}\right)\sin(k_\parallel a l)\end{aligned} \tag{10}$$

Evidently, the ED and MD lattice modes decouple when $T_{zy}(k_\parallel) = 0$, which occurs when $k_\parallel a l = m\pi$ for any integer m. This derivation of the ED−MD decoupling condition relies on the pairwise grouping of $\pm l$ terms as in the second line of eq 10, which is always possible in an infinite array. In finite arrays, the absence of perfect translation symmetry introduced by the array edges is expected to inhibit a strict decoupling of ED and

https://doi.org/10.1021/acs.jpcc.1c05024
J. Phys. Chem. C XXXX, XXX, XXX−XXX

MD modes among unit cells. Nevertheless, ED and MD modes are expected to remain approximately decoupled for finite arrays with large numbers of unit cells; although a recent work[39] has demonstrated that non-negligible cross coupling can persist at the array edges even for relatively large finite arrays of dielectric NPs.

Note that the ED−MD decoupling condition is satisfied when $k_{\|} = 0$, i.e., at the Γ point in reciprocal space, for integer $m = 0$. Previous studies of the LKE have investigated such situations with a normal angle of incidence where the ED and MD lattice modes are decoupled,[19−21] yet the far-field interferences remain. Such cases lead to strongly asymmetric forward versus backward scattering in the directions normal to the array, which produce the near-zero reflection associated with the LKE. While the Kerker beaming effect persists even when the ED and MD modes are coupled, the physics becomes particularly simple to understand when they are decoupled. Interestingly, the decoupling condition is also satisfied at the X point located at the edge of the Brillouin zone where $2k_{\|}$ is equal to $\pm$ |**K**|, where $\mathbf{K} = (2\pi/a)\hat{\mathbf{x}}$ is the primitive reciprocal lattice vector. Therefore, despite receiving much less attention in the literature, the conditions underlying the Γ point LKE also exist at each of the high-symmetry points in reciprocal space. The directional radiation beaming associated with the LKE is likewise also expected to occur at other high-symmetry points in reciprocal space, although with modified angular distributions since $k_{\|} \neq 0$.

To understand this generalization of the LKE, the differential scattering angular distributions are considered for arrays excited at the Γ and X points in reciprocal space. In general, the time-averaged power scattered into direction $\hat{\mathbf{n}}'$ is

$$\frac{dP}{d\Omega} = \frac{c}{8\pi}\mathrm{Re}\{r'^2\hat{\mathbf{n}}'\cdot[\mathbf{E}(\mathbf{r}') \times \mathbf{H}^*(\mathbf{r}')]\} \tag{11}$$

where $\mathbf{E}(\mathbf{r}')$ and $\mathbf{H}(\mathbf{r}')$ are the total electric and magnetic fields, respectively, at the observation point $\mathbf{r}' = r'\hat{\mathbf{n}}'$. In the case of a periodic array hosting electric $\mathbf{p}_l$ and magnetic $\mathbf{m}_l$ dipoles at each of the l sites

$$\mathbf{E}(\mathbf{r}') = \mathbf{E}^p(\mathbf{r}') + \mathbf{E}^m(\mathbf{r}') = \sum_l \mathbf{E}_l^p(\mathbf{r}') + \sum_l \mathbf{E}_l^m(\mathbf{r}') \tag{12}$$

where $\mathbf{E}_l^p(\mathbf{r}')$ and $\mathbf{E}_l^m(\mathbf{r}')$ represent the electric field produced by $\mathbf{p}_l$ and $\mathbf{m}_l$. The total magnetic field can be similarly partitioned into contributions sourced by the electric and magnetic dipoles. The explicit forms of each of contribution to the fields in the radiation zone are[40]

$$\begin{aligned}
\mathbf{E}_l^p(\mathbf{r}') &= \mu k_0^2[(\hat{\mathbf{n}}' \times \mathbf{p}_l) \times \hat{\mathbf{n}}']\frac{e^{ik|\mathbf{r}'-\mathbf{r}_l|}}{|\mathbf{r}'-\mathbf{r}_l|}\\
\mathbf{H}_l^p(\mathbf{r}') &= nk_0^2(\hat{\mathbf{n}}' \times \mathbf{p}_l)\frac{e^{ik|\mathbf{r}'-\mathbf{r}_l|}}{|\mathbf{r}'-\mathbf{r}_l|}\\
\mathbf{E}_l^m(\mathbf{r}') &= -\mu nk_0^2(\hat{\mathbf{n}}' \times \mathbf{m}_l)\frac{e^{ik|\mathbf{r}'-\mathbf{r}_l|}}{|\mathbf{r}'-\mathbf{r}_l|}\\
\mathbf{H}_l^m(\mathbf{r}') &= n^2k_0^2[(\hat{\mathbf{n}}' \times \mathbf{m}_l) \times \hat{\mathbf{n}}']\frac{e^{ik|\mathbf{r}'-\mathbf{r}_l|}}{|\mathbf{r}'-\mathbf{r}_l|}
\end{aligned} \tag{13}$$

Furthermore, in the radiation zone where $|\mathbf{r}'| \gg |\mathbf{r}_l|$ and the Fraunhofer approximation may be invoked,

$$\frac{e^{ik|\mathbf{r}'-\mathbf{r}_l|}}{|\mathbf{r}'-\mathbf{r}_l|} \approx \frac{e^{ikr'}}{r'}e^{-i\mathbf{k}'\cdot\mathbf{r}_l} \tag{14}$$

where $\mathbf{k}' = k\hat{\mathbf{n}}'$ is the wave vector associated with scattering into the observation direction. Under this approximation, the total fields sourced by each dipole type can be written as

$$\begin{aligned}
\mathbf{E}^p(\mathbf{r}') &= \mu k_0^2[(\hat{\mathbf{n}}' \times \hat{\mathbf{p}}) \times \hat{\mathbf{n}}']\frac{e^{ikr'}}{r'}\sum_l p_l e^{-i\mathbf{k}'\cdot\mathbf{r}_l}\\
\mathbf{H}^p(\mathbf{r}') &= nk_0^2(\hat{\mathbf{n}}' \times \hat{\mathbf{p}})\frac{e^{ikr'}}{r'}\sum_l p_l e^{-i\mathbf{k}'\cdot\mathbf{r}_l}\\
\mathbf{E}^m(\mathbf{r}') &= -\mu nk_0^2(\hat{\mathbf{n}}' \times \hat{\mathbf{m}})\frac{e^{ikr'}}{r'}\sum_l m_l e^{-i\mathbf{k}'\cdot\mathbf{r}_l}\\
\mathbf{H}^m(\mathbf{r}') &= n^2k_0^2[(\hat{\mathbf{n}}' \times \hat{\mathbf{m}}) \times \hat{\mathbf{n}}']\frac{e^{ikr'}}{r'}\sum_l m_l e^{-i\mathbf{k}'\cdot\mathbf{r}_l}
\end{aligned} \tag{15}$$

Provided the electric and magnetic dipoles at each site are driven by a plane wave source with a wave vector making projection $\mathbf{k}_{\|} = k_{\|}\hat{\mathbf{x}}$ onto the lattice direction, then $\xi_l = \xi e^{i\mathbf{k}_{\|}\cdot\mathbf{r}_l}$, $\xi = p, m$. Equation 15 can then be expressed as

$$\begin{aligned}
\mathbf{E}^p(\mathbf{r}') &= \mu k_0^2[(\hat{\mathbf{n}}' \times \mathbf{p}) \times \hat{\mathbf{n}}']\frac{e^{ikr'}}{r'}F(\hat{\mathbf{n}}', k_{\|})\\
\mathbf{H}^p(\mathbf{r}') &= nk_0^2(\hat{\mathbf{n}}' \times \mathbf{p})\frac{e^{ikr'}}{r'}F(\hat{\mathbf{n}}', k_{\|})\\
\mathbf{E}^m(\mathbf{r}') &= -\mu nk_0^2(\hat{\mathbf{n}}' \times \mathbf{m})\frac{e^{ikr'}}{r'}F(\hat{\mathbf{n}}', k_{\|})\\
\mathbf{H}^m(\mathbf{r}') &= n^2k_0^2[(\hat{\mathbf{n}}' \times \mathbf{m}) \times \hat{\mathbf{n}}']\frac{e^{ikr'}}{r'}F(\hat{\mathbf{n}}', k_{\|})
\end{aligned} \tag{16}$$

Using these expressions with eq 11, the total angular differential scattered power from the array can be written as

$$\frac{dP(\hat{\mathbf{n}}', k_{\|})}{d\Omega} = \left[\frac{dP_0(\hat{\mathbf{n}}')}{d\Omega}\right]|F(\hat{\mathbf{n}}', k_{\|})|^2 \tag{17}$$

where $[dP_0/d\Omega]$ is given by eq 3 and the structure factor $F(\hat{\mathbf{n}}', k_{\|})$ capturing the modulation of the angular distribution arising from diffraction is defined as

$$F(\hat{\mathbf{n}}', k_{\|}) = \sum_l e^{i(\mathbf{k}_{\|}-\mathbf{k}')\cdot\mathbf{r}_l} \tag{18}$$

where the sum is taken over all unit cells. Equation 17 provides a clear window into the physics of the LKE as it partitions the total differential scattering angular distribution into the product of $[dP_0/d\Omega]$, which ultimately depends only on the ED and MD polarizability tensors of a single unit cell, and the structure factor, which depends only upon the lattice geometry. For a finite 1D array of N unit cells with periodicity a, eq 18 becomes a geometric series that can be summed explicitly, leaving

$$|F(\hat{\mathbf{n}}', k_{\|})|^2 = \frac{\sin^2\left[\frac{N(k_{\|}'-k_{\|})a}{2}\right]}{\sin^2\left[\frac{(k_{\|}'-k_{\|})a}{2}\right]} \tag{19}$$

https://doi.org/10.1021/acs.jpcc.1c05024
J. Phys. Chem. C XXXX, XXX, XXX−XXX

LKE at Γ and X Reciprocal Space Points. First, the Γ point LKE is investigated for finite realizations of the 1D trimer array structure with periodicity a = 440 nm along the $\hat{\mathbf{x}}$ direction. Three different Γ point (i.e., $\mathbf{k}_{inc} \perp \hat{\mathbf{x}}$) excitation conditions, denoted I−III, are shown schematically in Figure 3a. It is well-understood that lattice plasmon polaritons capable of exhibiting ultranarrow spectral features are supported predominantly by far-field coupling of dipolar localized surface plasmon modes hosted by the NPs within each unit cell.[41,42] Excitation cases I−III were selected in order to probe the various possible ED/MD coupling schemes relative to the periodicity direction; the far-field radiation lobes of the ED and MD modes of each site are represented by the semitransparent blue and red shapes, respectively, in Figure 3a.

Extinction spectra calculated using the coupled ED method for finite realizations of the 1D structure with N = 251 unit cells are presented in Figure 3b. In case I, excitation of the trimer MD is forbidden due to symmetry since the incident wave vector is perpendicular to the trimer plane. Meanwhile the ED modes excited in each unit cell are along $\hat{\mathbf{x}}$ such that the ED far-fields are directed perpendicular from the array axis, which inhibits coupling between unit cells. Indeed, the case I extinction spectrum does not exhibit strong features arising from coupling to the Γ point diffraction mode near 440 nm, and the angular distribution (black) in the yz-plane in Figure 3c shows the expected equal forward versus backward scattering. Note that the observation angles θ' and ϕ' employed in Figure 3c are the usual spherical coordinate polar and azimuthal angles, respectively, in the coordinate system shown in Figure 3a. MD excitation is also prohibited by symmetry in excitation case II. However, far-field ED coupling takes place along the periodicity direction ($\hat{\mathbf{x}}$) in this situation, leading to the existence of strong lattice mode appearing in the extinction spectrum near 460 nm. Note that the small spectral feature near 440 nm observable in the case II spectrum is likely caused by simultaneous excitation of two ED trimer modes with different projections of the induced dipole moment onto the periodicity direction. As in case I, the angular distribution for case II in the xy-plane (blue) at λ = 460 nm exhibits no forward versus backward asymmetry; however, the angular distribution is strongly affected by diffraction at the Γ point as seen by the concentration of scattered light into the $\phi' = \pm \pi/2$ directions. In excitation case III, both ED and MD modes are accessible by the incident field, with long-range coupling of unit cells along the array supported by MD−MD coupling evidenced by the appearance of the spectrally narrow lattice mode near 440 nm. In this case, the angular distribution taken in the xz-plane clearly exhibits strong beaming of the scattered light into the forward direction along with nearly complete suppression of backscattered (i.e., reflected) light, the characteristic signature of the LKE. The beaming pattern in Figure 3c, calculated numerically using the coupled ED method with three spheres per unit cell, can be understood in light of eq 17 as the product of the modulus squared of the Γ point structure factor $|F(\theta', k_{\|} = 0)|^2$, shown in Figure 3c (inset) calculated using eq 19 with N = 251 unit cells, and $[dP_0/d\Omega]$ shown in Figure 1d.

To move beyond the specific case of the Γ point LKE studied previously by others and in Figure 3 of this paper, a new 1D lattice system is considered with periodicity a = 660 nm along $\hat{\mathbf{x}}$. The periodicity of this array was chosen such that the X point ($k_{\|} = \pm \pi/a$) band edge states occur slightly red-shifted with respect to the empty-lattice X points occurring at

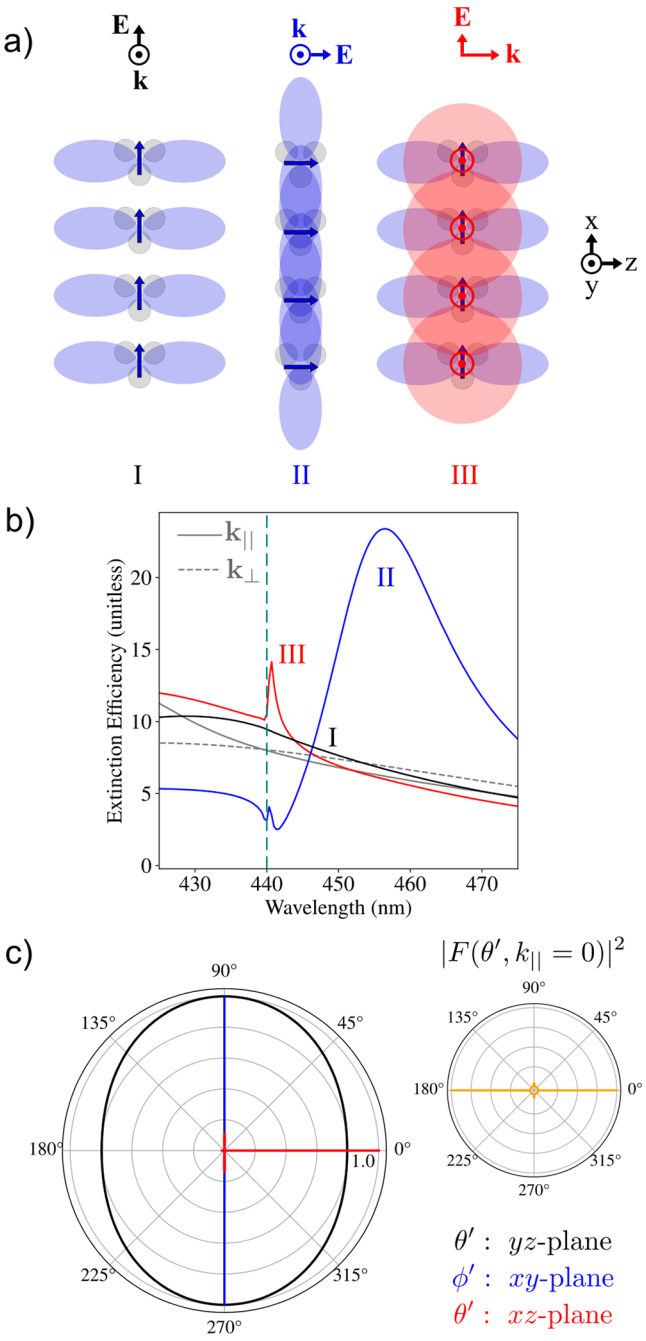

Figure 3. Diffractively coupled lattice modes supported by a 1D array of trimers excited at the Γ point. (a) Schematic depiction of three different Γ point excitation geometries with the orientations of ED and MD far-field dipole radiation patterns shown in blue and red, respectively. (b) Extinction efficiency spectra calculated using the coupled ED method for finite realizations of an a = 440 nm periodicity 1D array with 251 unit cells excited under conditions I−III shown in panel (a). Extinction spectra of the isolated trimer structure are shown as solid and dashed gray lines for the $\mathbf{k}_{\|}$ and $\mathbf{k}_{\perp}$ excitation conditions, respectively, of Figure 1. The vertical dashed line marks the spectral position of the Rayleigh anomaly. (c) Differential scattered power angular plots within specific Cartesian planes for excitation cases I−III noted in the legend. Each angular distribution was calculated using finite arrays with N = 251 unit cells and λ = 441, 460, and 441 nm, respectively, for cases I−III. The inset shows the squaredmodulus of the Γ point structure factor $|F(\theta', k_{\|} = 0)|^2$ calculated analytically using eq 19 with N = 251.

https://doi.org/10.1021/acs.jpcc.1c05024
J. Phys. Chem. C XXXX, XXX, XXX−XXX

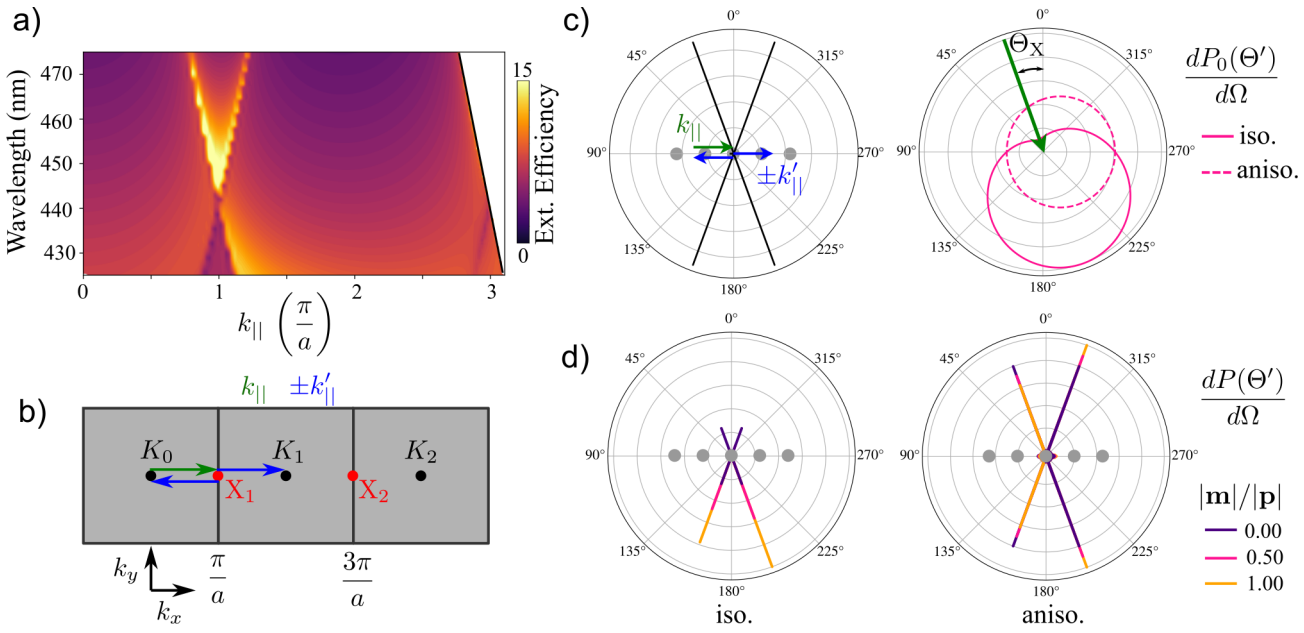

Figure 4. X point lattice Kerker effect. (a) Extinction efficiency spectra as a function of $k_{||}$ for a finite 1D array with periodicity a = 660 nm and N = 251 unit cells. The X point band-edge mode near λ = 445 nm and $k_{||} = \pi/a$ is nearly degenerate with the various Γ point modes supported by the array considered in Figure 3. (b) Diagrammatic representation of reciprocal space illustrating the von Laue diffraction condition for $k_{||}$ at the X point (green arrow) is satisfied for equal and opposite observation directions (blue arrows). Points belonging to the reciprocal lattice are labeled as K_m. (c) Angular plot of $|F(\Theta', k_{||} = \pi/a)|^2$ (black) showing the four-lobed pattern dictated by the von Laue diffraction condition. The angular plot to the right shows differential scattered power distributions for an individual scatterer with isotropic (solid) and planar anisotropic (dashed) MD polarizability when excited at Θ_X = 20° and $|\mathbf{m}|/|\mathbf{p}|$ = 0.5. The green arrow indicates the direction of the incident wave vector. (d) Differential scattered power distributions for 1D finite arrays with N = 251 unit cells at the X point calculated using eq 17 and $|\mathbf{m}|/|\mathbf{p}|$ ranging from zero to unity. The MD polarizability is isotropic (anisotropic) in the left (right) plot.

440 nm, since this is degenerate with the Γ point diffractive mode considered in Figure 3. Therefore, for comparison, a fixed detuning is maintained between the normal modes supported by the trimer and the Γ and X point diffractive modes. The extinction spectrum of this array is plotted in Figure 4a as a function of in-plane Bloch vector $k_{||}$ and incident wavelength, confirming the existence of a band edge lattice mode near λ = 445 nm at $k_{||} = \pi/a$. Following excitation by a plane wave with incident wave vector projection $\mathbf{k}_{||}$ onto the periodicity direction, constructive interference is achieved into directions satisfying the von Laue diffraction condition[30,43] $\mathbf{k}_{||} - \mathbf{k}'_{||} = m\mathbf{K}$, where m is an integer, $\mathbf{K} = (2\pi/a)\hat{\mathbf{x}}$ is the primitive reciprocal lattice vector, and $\mathbf{k}'_{||}$ is the in-plane component of the scattered wave vector into the observation direction $\hat{\mathbf{n}}'$. Note that this condition is identical to that which causes the denominator of eq 19 to become zero and where the squared modulus of the structure factor attains its maximum value. Figure 4b presents a pictorial representation of the 1D reciprocal space lattice with the von Laue condition satisfied by equal and opposite $\mathbf{k}'_{||}$ vectors for $k_{||}$ at the X point. Therefore, in contrast to the situation at the Γ point where $|F(\hat{\mathbf{n}}', k_{||} = 0)|^2$ is strongly peaked only along the forward and backward directions (see Figure 3c), at the X point $|F(\hat{\mathbf{n}}', k_{||} = \pi/a)|^2$ exhibits a four-lobed pattern with each lobe centered at $\pm\theta' = \sin^{-1}(\lambda k_{||}/2\pi n) \sim \pm 20°$ from the direction normal to the periodicity as shown in Figure 4c.

In addition to the $k_{||}$-dependence arising from the structure factor in eq 17, the total differential scattering angular distribution also depend on the trimer ED and MD polarizability tensors through $[dP_0/d\Omega]$. This factor is of critical importance since the MD polarizability tensor of a planar plasmonic oligomer is highly anisotropic with only a single nonzero component, which in the present case is $\ddot{\boldsymbol{\alpha}}_m^{\text{aniso}}(\omega) = \alpha_m(\omega)\hat{\mathbf{y}} \otimes \hat{\mathbf{y}}$. In particular, for an incident plane wave polarized along $\hat{\mathbf{z}}$ and wave vector within the xy-plane, $\mathbf{m} = \ddot{\boldsymbol{\alpha}}_m^{\text{aniso}} \cdot \mathbf{H}_0 = \alpha_m^{\text{aniso}}|\mathbf{H}_0|\sin\Theta\hat{\mathbf{y}}$, where $\Theta = \phi - 90°$. With this definition, Θ = 0° corresponds to the case II Γ point excitation condition of Figure 3 and the amplitude of the induced MD is maximized at Θ = 90°, which corresponds to θ = 0° in Figure 1. Meanwhile, the magnitude of the induced ED is independent of Θ. Consequently, although $(|\mathbf{m}|/|\mathbf{p}|)_{\Theta=90°} \approx 0.5$ for the trimer structure for the $\mathbf{k}_{||}$ excitation condition of Figure 1, $(|\mathbf{m}|/|\mathbf{p}|)_{\Theta_X} = (|\mathbf{m}|/|\mathbf{p}|)_{\Theta=90°}\sin\Theta_X$ at the X point, where Θ_X = 20°. This reduces the value of $(|\mathbf{m}|/|\mathbf{p}|)_{\theta_X}$ and diminishes the asymmetry in the $[dP_0/d\Omega]$ scattering distribution shown in Figure 4c (dashed) as compared to what occurs for structures such as spherical high-index dielectric NPs or plasmonic metamolecule structures[33,44] with isotropic MD polarizability tensors $\ddot{\boldsymbol{\alpha}}_m^{\text{iso}}(\omega) = \alpha^{\text{iso}}(\omega)\ddot{\boldsymbol{I}}$ (solid), where $(|\mathbf{m}|/|\mathbf{p}|)$ is independent of the incident angle.

According to eq 17, the total angular scattering distribution arising from the array structure is simply the product of the two angular plots in Figure 4c. The resulting total differential angular scattering distributions for 1D arrays of scatterers with isotropic (anisotropic) MD polarizability tensors excited at the X point is presented on the left (right) side of Figure 4d for $(|\mathbf{m}|/|\mathbf{p}|)_{\Theta=90°}$ ratios varying from zero (pure ED scattering) to unity. Each angular distribution is normalized to the maximum differential scattered power for $(|\mathbf{m}|/|\mathbf{p}|)_{\Theta=90°} = 1$, and the

https://doi.org/10.1021/acs.jpcc.1c05024
J. Phys. Chem. C XXXX, XXX, XXX−XXX

order of stacking for traces for $\Theta < 180°$ is inverted relative to that for $\Theta > 180°$ for the anisotropic MD polarizability case to ensure visibility of all traces. The strong forward-beaming of radiation associated with the Γ point LKE persists at the X point in the case of isotropic MD polarizabilities, with a slight asymmetry between the two radiation lobes separated by ∼40°. Meanwhile, in the case of anisotropic MD polarizabilities, strong beaming into the forward direction is replaced by a weaker beaming along the $\mathbf{k}_{\|}$ direction.

Finally, the spatial distributions of the electric and magnetic response fields are considered for the 1D trimer arrays of Figures 3 and 4 excited at the case III Γ and X points, respectively. Figure 5a shows the out-of-plane component of

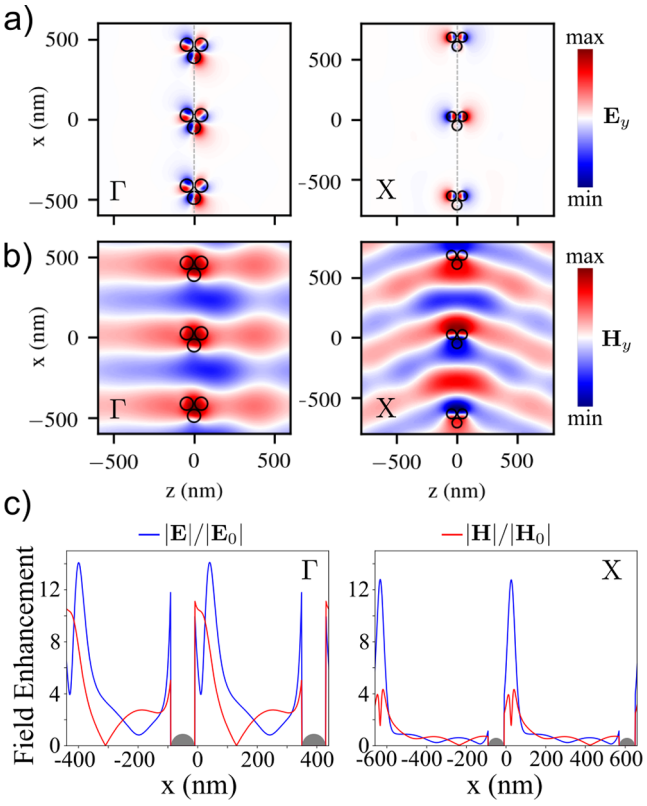

Figure 5. Γ and X point response fields. (a) and (b) are the out-of-plane components of the response E- and H-fields, respectively, excited at the case III Γ point (left) and X point (right). Note that the array period is a = 440 nm (660 nm) for the left (right) plot. The field maximum and minimum values are not equal for the left and right plots within each panel. (c) Total E- and H-field enhancement along the array axis (dashed line in panel a) for Γ and X point excitation cases on the left and right, respectively. Gray hemispheres indicate regions within NP interiors.

the response electric field ($\mathbf{E}_y$) in a plane displaced 5 nm above the top surface of the NPs along the y-direction for three unit cells at the center of finite arrays of N = 251 unit cells. For case III Γ point excitation of the a = 440 nm array, the induced EDs within each trimer unit cell are arranged head-to-tail in clear qualitative similarity to what is shown in Figure 2b, though at the wavelength λ = 441 nm of the MD-coupled lattice mode. It is also evident that the unit cell responses are all in-phase. In contrast, the plot on the right of Figure 5a shows that adjacent unit cells of the a = 660 nm array are, as anticipated, π out-of-phase when excited at the X point. Additionally, strong z-oriented EDs are induced in the top two NPs, while a weaker ED oriented in the opposite direction is induced in lower NP within each unit cell. The situation is similar for the magnetic response fields presented in Figure 5b; the H-field within each a = 440 nm unit cell are in-phase and similar to the MD mode illustrated in the bottom panel of Figure 2b. The spatial distribution of the H-field in the right panel of Figure 5b also displays a π phase shift between adjacent unit cells, although the distribution of the field within each unit cell is more similar to what is expected from two longitudinally coupled EDs rather than the trimer MD mode. This is attributed to the weak MD mode excitation at the X point arising from the aniostropic MD polarizability tensor discussed above. Figure 5c shows the total E- and H-field enhancements along the x-axis across two unit cells at the center of the two arrays shown in panel (a). As expected, the left plot indicates modest enhancement of the E-field and stronger enhancement of the H-field for the a = 440 nm array excited at the Γ point, while the situation is reversed for the plot on the right for the a = 660 nm array excited at the X point. The enhanced H-fields evident in the Γ point case on the left could, for example, be leveraged to achieve lasing from quantum emitters supporting MD transitions in the spirit of related plasmonic nano laser systems operating with dye molecules supporting ED transitions.[45]

CONCLUSIONS

In conclusion, periodic arrays of diffractively coupled plasmonic oligomer structures exhibit the lattice Kerker effect analogous to previously studied array structures of high-index dielectric nanoparticles. In particular, under suitable normal incidence conditions where both the ED and MD modes supported by oligomers within each unit cell can couple to incident radiation, a strong forward-directed radiation beaming is demonstrated numerically for 1D arrays of plasmonic trimers composed of Ag nanoparticles. The numerical results from the coupled electric dipole model for the 1D non-Bravais trimer array are rationalized using a coupled electric and magnetic dipole model on a 1D Bravais lattice, allowing differential scattered power angular distributions from the array to be decomposed into the product of the angular distribution produced by a single unit cell containing colocalized electric and magnetic dipoles and the squared modulus of a structure factor accounting for diffraction arising from the periodic array. Furthermore, this work extends previous studies of the lattice Kerker effect at the Γ point, enabling the consideration of the lattice Kerker effect at arbitrary points in reciprocal space. In particular, it is shown that ED and MD lattice modes decouple at the X point, where manifestations of the lattice Kerker effect are compared and contrasted for 1D arrays with isotropic and anisotropic magnetic polarizability tensors.

ASSOCIATED CONTENT

Supporting Information

The Supporting Information is available free of charge at https://pubs.acs.org/doi/10.1021/acs.jpcc.1c05024.

Additional calculations for a single 80 nm diameter Ag sphere and the individual trimer structure including higher-order multipoles beyond the electric and magnetic dipoles. Decomposition of the scattered power spectrum from the individual trimer into ED and MD contributions (PDF)

https://doi.org/10.1021/acs.jpcc.1c05024
J. Phys. Chem. C XXXX, XXX, XXX−XXX

AUTHOR INFORMATION

Corresponding Author

David J. Masiello − *Department of Chemistry, University of Washington, Seattle, Washington 98195, United States;* orcid.org/0000-0002-1187-0920; Email: masiello@uw.edu

Authors

Marc R. Bourgeois − *Department of Chemistry, University of Washington, Seattle, Washington 98195, United States;* orcid.org/0000-0002-9435-9051

Andrew W. Rossi − *Department of Chemistry, University of Washington, Seattle, Washington 98195, United States*

Matthieu Chalifour − *Department of Physics, University of Washington, Seattle, Washington 98195, United States*

Charles Cherqui − *Department of Chemistry, Northwestern University, Evanston, Illinois 60208, United States;* orcid.org/0000-0003-2818-7973

Complete contact information is available at: https://pubs.acs.org/10.1021/acs.jpcc.1c05024

Notes

The authors declare no competing financial interest.

ACKNOWLEDGMENTS

M.R.B., C.C., and D.J.M. are grateful for their time spent under the mentorship of professor George C. Schatz. His encouragement and passion for science have made this work, and countless others, possible. Work at the University of Washington was supported by the U.S. National Science Foundation under Award CHE-1954393 (M.R.B., A.W.R., M.C., D.J.M.). Work at the Northwestern University was supported by a Department of Energy Grant under award DE-SC0004752 (C.C.).

REFERENCES

(1) Kerker, M.; Wang, D. S.; Giles, C. L. Electromagnetic Scattering by Magnetic Spheres. *J. Opt. Soc. Am.* **1983**, *73*, 765−767.

(2) Liu, W.; Kivshar, Y. S. Generalized Kerker Effects in Nanophotonics and Meta-Optics. *Opt. Express* **2018**, *26*, 13085−13105.

(3) Monticone, F.; Alù, A. The Quest for Optical Magnetism: from Split-Ring Resonators to Plasmonic Nanoparticles and Nanoclusters. *J. Mater. Chem. C* **2014**, *2*, 9059−9072.

(4) Merlin, R. Metamaterials and the Landau−Lifshitz Permeability Argument: Large Permittivity Begets High-Frequency Magnetism. *Proc. Natl. Acad. Sci. U. S. A.* **2009**, *106*, 1693−1698.

(5) Evlyukhin, A. B.; Novikov, S. M.; Zywietz, U.; Eriksen, R. L.; Reinhardt, C.; Bozhevolnyi, S. I.; Chichkov, B. N. Demonstration of Magnetic Dipole Resonances of Dielectric Nanospheres in the Visible Region. *Nano Lett.* **2012**, *12*, 3749−3755.

(6) Alù, A.; Salandrino, A.; Engheta, N. Negative Effective Permeability and Left-Handed Materials at Optical Frequencies. *Opt. Express* **2006**, *14*, 1557−1567.

(7) Brandl, D. W.; Mirin, N. A.; Nordlander, P. Plasmon Modes of Nanosphere Trimers and Quadrumers. *J. Phys. Chem. B* **2006**, *110*, 12302−12310.

(8) Sheikholeslami, S. N.; García-Etxarri, A.; Dionne, J. A. Controlling the Interplay of Electric and Magnetic Modes via Fano-Like Plasmon Resonances. *Nano Lett.* **2011**, *11*, 3927−3934.

(9) Cherqui, C.; Bigelow, N. W.; Vaschillo, A.; Goldwyn, H.; Masiello, D. J. Combined Tight-Binding and Numerical Electrodynamics Understanding of the STEM/EELS Magneto-Optical Responses of Aromatic Plasmon-Supporting Metal Oligomers. *ACS Photonics* **2014**, *1*, 1013−1024.

(10) Cherqui, C.; Wu, Y.; Li, G.; Quillin, S. C.; Busche, J. A.; Thakkar, N.; West, C. A.; Montoni, N. P.; Rack, P. D.; Camden, J. P.; et al. STEM/EELS Imaging of Magnetic Hybridization in Symmetric and Symmetry-Broken Plasmon Oligomer Dimers and All-Magnetic Fano Interference. *Nano Lett.* **2016**, *16*, 6668−6676.

(11) Montoni, N. P.; Quillin, S. C.; Cherqui, C.; Masiello, D. J. Tunable Spectral Ordering of Magnetic Plasmon Resonances in Noble Metal Nanoclusters. *ACS Photonics* **2018**, *5*, 3272−3281.

(12) Alaee, R.; Filter, R.; Lehr, D.; Lederer, F.; Rockstuhl, C. A Generalized Kerker Condition for Highly Directive Nanoantennas. *Opt. Lett.* **2015**, *40*, 2645−2648.

(13) Liu, W.; Kivshar, Y. S. Multipolar Interference Effects in Nanophotonics. *Philos. Trans. R. Soc., A* **2017**, *375*, 20160317.

(14) Coenen, T.; Arango, F. B.; Koenderink, A. F.; Polman, A. Directional Emission from a Single Plasmonic Scatterer. *Nat. Commun.* **2014**, *5*, 3250.

(15) Paniagua-Domínguez, R.; Yu, Y. F.; Miroshnichenko, A. E.; Krivitsky, L. A.; Fu, Y. H.; Valuckas, V.; Gonzaga, L.; Toh, Y. T.; Kay, A. Y. S.; Luk'yanchuk, B.; et al. Generalized Brewster Effect in Dielectric Metasurfaces. *Nat. Commun.* **2016**, *7*, 10362.

(16) Lunnemann, P.; Koenderink, A. F. Dispersion of Guided Modes in Two-Dimensional Split Ring Lattices. *Phys. Rev. B: Condens. Matter Mater. Phys.* **2014**, *90*, 245416.

(17) Yu, N.; Capasso, F. Flat Optics with Designer Metasurfaces. *Nat. Mater.* **2014**, *13*, 139−150.

(18) Aieta, F.; Kats, M. A.; Genevet, P.; Capasso, F. Multiwavelength Achromatic Metasurfaces by Dispersive Phase Compensation. *Science* **2015**, *347*, 1342−1345.

(19) Babicheva, V. E.; Evlyukhin, A. B. Resonant Lattice Kerker Effect in Metasurfaces with Electric and Magnetic Optical Responses. *Laser Photonics Rev.* **2017**, *11*, 1700132.

(20) Babicheva, V. E.; Evlyukhin, A. B. Metasurfaces with Electric Quadrupole and Magnetic Dipole Resonant Coupling. *ACS Photonics* **2018**, *5*, 2022−2033.

(21) Gerasimov, V.; Ershov, A.; Bikbaev, R.; Rasskazov, I.; Isaev, I.; Semina, P.; Kostyukov, A.; Zakomirnyi, V.; Polyutov, S.; Karpov, S. Plasmonic Lattice Kerker Effect in Ultraviolet-Visible Spectral Range. *Phys. Rev. B: Condens. Matter Mater. Phys.* **2021**, *103*, 035402.

(22) Kwadrin, A.; Koenderink, A. F. Diffractive Stacks of Metamaterial Lattices with a Complex Unit Cell: Self-Consistent Long-Range Bianisotropic Interactions in Experiment and Theory. *Phys. Rev. B: Condens. Matter Mater. Phys.* **2014**, *89*, 045120.

(23) Esposito, M.; Todisco, F.; Bakhti, S.; Passaseo, A.; Tarantini, I.; Cuscunà, M.; Destouches, N.; Tasco, V. Symmetry Breaking in Oligomer Surface Plasmon Lattice Resonances. *Nano Lett.* **2019**, *19*, 1922−1930.

(24) Baur, S.; Sanders, S.; Manjavacas, A. Hybridization of Lattice Resonances. *ACS Nano* **2018**, *12*, 1618−1629.

(25) Zundel, L.; May, A.; Manjavacas, A. Lattice Resonances Induced by Periodic Vacancies in Arrays of Nanoparticles. *ACS Photonics* **2021**, *8*, 360−368.

(26) Guo, R.; Hakala, T. K.; Törmä, P. Geometry Dependence of Surface Lattice Resonances in Plasmonic Nanoparticle Arrays. *Phys. Rev. B: Condens. Matter Mater. Phys.* **2017**, *95*, 155423.

(27) Li, R.; Bourgeois, M. R.; Cherqui, C.; Guan, J.; Wang, D.; Hu, J.; Schaller, R. D.; Schatz, G. C.; Odom, T. W. Hierarchical Hybridization in Plasmonic Honeycomb Lattices. *Nano Lett.* **2019**, *19*, 6435−6441.

(28) Guo, R.; Nečada, M.; Hakala, T. K.; Väkeväinen, A. I.; Törmä, P. Lasing at K Points of a Honeycomb Plasmonic Lattice. *Phys. Rev. Lett.* **2019**, *122*, 013901.

(29) Guan, J.; Sagar, L. K.; Li, R.; Wang, D.; Bappi, G.; Watkins, N. E.; Bourgeois, M. R.; Levina, L.; Fan, F.; Hoogland, S.; et al. Engineering Directionality in Quantum Dot Shell Lasing Using Plasmonic Lattices. *Nano Lett.* **2020**, *20*, 1468−1474.

(30) Guan, J.; Bourgeois, M. R.; Li, R.; Hu, J.; Schaller, R. D.; Schatz, G. C.; Odom, T. W. Identification of Brillouin Zones by In-Plane Lasing from Light-Cone Surface Lattice Resonances. *ACS Nano* **2021**, *15*, 5567−5573.

(31) Terekhov, P. D.; Baryshnikova, K. V.; Artemyev, Y. A.; Karabchevsky, A.; Shalin, A. S.; Evlyukhin, A. B. Multipolar Response of Nonspherical Silicon Nanoparticles in the Visible and Near-Infrared Spectral Ranges. *Phys. Rev. B: Condens. Matter Mater. Phys.* **2017**, *96*, 035443.
(32) Hentschel, M.; Dregely, D.; Vogelgesang, R.; Giessen, H.; Liu, N. Plasmonic Oligomers: the Role of Individual Particles in Collective Behavior. *ACS Nano* **2011**, *5*, 2042−2050.
(33) Bourgeois, M. R.; Liu, A. T.; Ross, M. B.; Berlin, J. M.; Schatz, G. C. Self-Assembled Plasmonic Metamolecules Exhibiting Tunable Magnetic Response at Optical Frequencies. *J. Phys. Chem. C* **2017**, *121*, 15915−15921.
(34) Johnson, P. B.; Christy, R.-W. Optical Constants of the Noble Metals. *Phys. Rev. B* **1972**, *6*, 4370−4379.
(35) Quillin, S. C.; Cherqui, C.; Montoni, N. P.; Li, G.; Camden, J. P.; Masiello, D. J. Imaging Plasmon Hybridization in Metal Nanoparticle Aggregates with Electron Energy-Loss Spectroscopy. *J. Phys. Chem. C* **2016**, *120*, 20852−20859.
(36) Pakeltis, G.; Rotunno, E.; Khorassani, S.; Garfinkel, D. A.; Collette, R.; West, C. A.; Retterer, S. T.; Idrobo, J. C.; Masiello, D. J.; Rack, P. D. High Spatial and Energy Resolution Electron Energy Loss Spectroscopy of the Magnetic and Electric Excitations in Plasmonic Nanorod Oligomers. *Opt. Express* **2021**, *29*, 4661−4671.
(37) Mackowski, D. W.; Mishchenko, M. I. Calculation of the T Matrix and the Scattering Matrix for Ensembles of Spheres. *J. Opt. Soc. Am. A* **1996**, *13*, 2266−2278.
(38) Mackowski, D.; Mishchenko, M. A. Multiple Sphere T-Matrix Fortran Code for Use on Parallel Computer Clusters. *J. Quant. Spectrosc. Radiat. Transfer* **2011**, *112*, 2182−2192.
(39) Zakomirnyi, V.; Ershov, A.; Gerasimov, V.; Karpov, S.; Ågren, H.; Rasskazov, I. Collective Lattice Resonances in Arrays of Dielectric Nanoparticles: a Matter of Size. *Opt. Lett.* **2019**, *44*, 5743−5746.
(40) Jackson, J. D. *Classical Electrodynamics*, Third ed.; John Wiley & Sons, Inc.: New York, 1999.
(41) Zou, S.; Janel, N.; Schatz, G. C. Silver Nanoparticle Array Structures that Produce Remarkably Narrow Plasmon Lineshapes. *J. Chem. Phys.* **2004**, *120*, 10871−10875.
(42) Cherqui, C.; Bourgeois, M. R.; Wang, D.; Schatz, G. C. Plasmonic Surface Lattice Resonances: Theory and Computation. *Acc. Chem. Res.* **2019**, *52*, 2548−2558.
(43) Ashcroft, N. W.; Mermin, N. D. *Solid State Physics*; Holt-Saunders: New York, 1976.
(44) Qian, Z.; Hastings, S. P.; Li, C.; Edward, B.; McGinn, C. K.; Engheta, N.; Fakhraai, Z.; Park, S.-J. Raspberry-Like Metamolecules Exhibiting Strong Magnetic Resonances. *ACS Nano* **2015**, *9*, 1263−1270.
(45) Zhou, W.; Dridi, M.; Suh, J. Y.; Kim, C. H.; Co, D. T.; Wasielewski, M. R.; Schatz, G. C.; Odom, T. W. Lasing Action in Strongly Coupled Plasmonic Nanocavity Arrays. *Nat. Nanotechnol.* **2013**, *8*, 506−511.

https://doi.org/10.1021/acs.jpcc.1c05024
J. Phys. Chem. C XXXX, XXX, XXX−XXX